A Small-AC-Signal Injection-Based Decentralized Secondary Frequency Control for Droop-Controlled Islanded Microgrids

Baojin Liu, *Member, IEEE*, Teng Wu, Zeng Liu, *Member, IEEE*, and Jinjun Liu, *Fellow, IEEE*

***Abstract*—In an islanded microgrid composed of droop-controlled parallel inverters, the system frequency endures deviations as the load changes. To compensate for frequency deviation without involving communication infrastructures among distributed generators (DGs), the proportional-integral regulator based secondary frequency control (PI-SFC) method has been proposed in the literature. However, PI-SFC may incur real power-sharing errors because the integrator accumulates disturbances and noise in each DG, leading to different compensation values of nominal real power. To achieve frequency restoration while maintaining equal real power sharing among DGs, this article proposes a small-ac-signal injection-based secondary frequency control (SACS-SFC) method, which is implemented by injecting an additional ac signal into the output voltage of each DG. Furthermore, a droop relation between the frequency of the injected SACS and the compensation value of nominal real power is innovatively established to trim the output real power of each DG to be equal. Frequency deviations caused by primary droop control are thus eliminated, and even real power sharing can be maintained among DGs. Moreover, the control parameters of the proposed SACS-SFC are comprehensively designed via steady state and dynamic model of the system. Simulation and experimental results demonstrate the effectiveness of the proposed method.**

***Index Terms*—Decentralized secondary control, droop control, frequency restoration, microgrid, real power sharing, signal injection.**

I. Introduction

MICROGRID is a relatively new concept born out of growing concern for the environment and energy crisis. It is an integrated energy system consisting of interconnected loads and distributed generators (DGs) [1]–[3]. In most cases, all DGs in a microgrid are linked to the point of common coupling (PCC) through power electronic interfaces such as inverters [4], [5]. Thus, control of parallel inverters is highly important in the study of microgrids.

To endow microgrids with intelligence and flexibility, a hierarchical control structure consisting of three levels, i.e., primary control, secondary control, and tertiary control, has been widely applied in microgrid control [3], [6], [7]. Primary control maintains voltage and frequency stability and provides real and reactive power-sharing control for DGs. Secondary control can restore the frequency and voltage deviations produced by operation of primary controls. Tertiary control manages power flow between the microgrid and main grid and facilitates economically optimal operation. This article focuses on frequency restoration, which falls under secondary control.

In primary control, the real power-frequency (P-ω) and reactive power-voltage amplitude (Q-E) droop control method has been found to be superior due to advantages such as high flexibility, reliability, and power-sharing capability without using communication links among DGs [3], [8], [9]. However, the conventional droop method suffers from a major problem involving frequency and voltage amplitude deviations, which result from the inherent tradeoff between power-sharing accuracy and the voltage regulation rate. Secondary frequency control (SFC) methods have been commonly used to mitigate frequency deviations introduced by droop control [6], [10]–[29]. Based on the control architecture, secondary control schemes can be broadly categorized into centralized, distributed, and decentralized schemes [10].

Under a centralized secondary control strategy, a microgrid central controller (MGCC) collects information from the PCC and restores frequency by a proportional-integral (PI) controller. Then, the output compensation signal of the PI controller is sent to local controllers of each DG via communication links [6], [11]. The centralized approaches can achieve accurate frequency restoration with a simple control structure. However, dependence on MGCC and one-to-all communication structure reduces system reliability, because the breakdown of MGCC or communication can lead to collapse of the whole microgrid. Moreover, the MGCC and communication links increase the costs and deteriorate the plug-and-play functionalities of the system.

To eliminate the dependence on MGCC and improve system reliability, distributed secondary control schemes have thus been proposed, which are implemented in DG local controllers with

Manuscript received September 17, 2019; revised January 20, 2020; accepted March 16, 2020. Date of publication March 29, 2020; date of current version July 20, 2020. This work was supported by the National Natural Science Foundation of China under Grant 51437007. Recommended for publication by Associate Editor H. L. Ginn. *(Corresponding authors: Zeng Liu and Jinjun Liu.)*

Baojin Liu, Zeng Liu, and Jinjun Liu are with the State Key Lab of Electrical Insulation and Power Equipment, School of Electrical Engineering, Xi'an Jiaotong University, Xi'an 710049, China (e-mail: liubaojin.pe@gmail.com; zengliu@xjtu.edu.cn; jjliu@xjtu.edu.cn).

Teng Wu was with the State Key Lab of Electrical Insulation and Power Equipment, School of Electrical Engineering, Xi'an Jiaotong University, Xi'an 710049, China. He is now with the Power Electronics Products COE (Center of Excellence), Envision Energy Co., Ltd., Shanghai 200050, China (e-mail: wuteng008@yeah.net).

Color versions of one or more of the figures in this article are available online at http://ieeexplore.ieee.org.

Digital Object Identifier 10.1109/TPEL.2020.2983878

the help of DG-to-DG communications [12]–[22]. Averaging-based [12], [13] and consensus-based [14]–[18] techniques are two representative distributed methods. In averaging-based secondary control, each DG measures its frequency and sends it to all or some other DGs, and calculates the average frequency. Then, this average value is compensated to the rated frequency by a secondary algorithm in the DG local controller [12], [13]. Although a MGCC is no longer required, averaging based methods demand massive communication links with high bandwidth. The consensus-based algorithms were proposed based on the multiagent system theory, which realize the frequency restoration by exchanging information between an agent (DG) and some of its neighbors [14]–[18]. Consensus-based methods reduce the complexity of communication architecture by requiring only neighbor-to-neighbor interactions. However, any fault in DG or communication links still affects the overall coordination if there is not enough redundant communication links. In addition, some other distributed secondary control methods were proposed recently trying to further reduce the communication complexity and increase system robustness. For instance, distributed SFC methods based on unidirectional low-bandwidth communications appeared in [19] and [20], distributed phasor measurement units were employed in [21], and a new maximum power loading factor concept was proposed in [22] to realize the frequency restoration with low bandwidth communication. However, all these aforementioned distributed control strategies still rely on communication links, which endure low reliability and high costs.

To realize the SFC only based on DG local variables and completely eliminate communication links among DGs, decentralized schemes were presented in [23]–[29], which can be classified as proportional-regulator based (P-SFC) schemes [23], [24] and PI-regulator based (PI-SFC) schemes [25]–[28] according to the form of controller. A secondary controller consisting of a proportional regulator for frequency restoration was introduced in [23]. Similarly, the secondary frequency controller in [24] was a low-pass filter (LPF), which has an approximate characteristic as a proportional regulator at low frequencies. These P-SFC methods generate same compensation value, therefore maintaining real power sharing achieved by the primary controller. However, they cannot fully restore frequency to the rated value. To handle this issue, a PI-SFC method was adopted for frequency restoration in a communicationless manner in [25]. In [26], a washout-filter based control method was proposed to eliminate frequency deviations, which actually is equivalent to the PI-SFC [27]. In [28], an adaptive inverse control scheme was proposed based on the least mean square (LMS) algorithm to maintain frequency at the rated value, which can be regarded as an integral regulator with integration gain adaptively modified by the LMS algorithm. In contrast to P-SFC methods, PI-SFC can fully restore the frequency with the help of integrator, but even power sharing among inverters cannot be guaranteed because the output of the integral regulator is closely related to the process of integration. The integrators in each DG accumulate different disturbances and noise and then produce different output values; therefore, power sharing deteriorates gradually. To combine the advantages of P-SFC and PI-SFC, Rey *et al.* [29] proposed a switched secondary controller, in which P-SFC and PI-SFC are adopted successively according to a predefined time protocol. This method can realize frequency restoration and even real power sharing concurrently without any communication links. However, the switch of control scheme highly depends on the event detection strategy. A failure in the event detection can worsen the system performance and even lead to oscillations.

In light of cost and reliability, decentralized secondary control schemes that are independent on MGCC or communication links are more attractive than the centralized and distributed methods. However, all the existing decentralized methods have limitations. P-SFC cannot fully restore frequency to the rated value, PI-SFC deteriorates real power sharing, and the switched secondary controller has the risk of switching failure. To solve all these limitations, this article modifies the PI-SFC into a small-ac-signal injection-based SFC (SACS-SFC), whose distinctive feature is to inject an additional ac signal into the output voltage of each DG. The concept of injecting SACS was first presented in [30] and [31] to enhance the power-sharing performance in the case of imbalanced feeder impedance and was later employed in dc microgrids to improve the current-sharing accuracy [32]. Inspired by this idea, this article adopts SACS to manage the real power-sharing problem resulting from the frequency restoration process of PI-SFC. Note that the idea of SACS-SFC was proposed by Wu *et al.* [33] with only brief introduction of basic idea and very preliminary verifications. However, in this article, we have added detailed explanation of the operation principle, selection of the SACS frequency and amplitude, design methodology of control parameters based on steady-state analysis and dynamic system modeling, and more comprehensive simulation and experimental results.

The main contribution of this article is summarized as follows. First, similar to PI-SFC, a PI regulator is employed to adjust the nominal real power of the primary droop control to fully restore system frequency. Hence, the limitation of P-SFC is avoided. Second, the compensation values in each DG are further trimmed to be equal for even real power sharing by introducing an additional SACS droop control. So the demerit of PI-SFC is overcome. Third, compared with the switched secondary controller in [29], the proposed method does not need to change the control algorithm during the operation. Thus, the risk of controller switching failure is eliminated. Last but not the least, the parameter design of the secondary controller is comprehensively introduced based on steady state and dynamic model of the proposed SACS-SFC.

The remainder of this article is organized as follows. Section II briefly reviews the operation principle and limitation of primary droop control and PI-SFC. In Section III, the proposed SACS-SFC is explained in detail. In Section IV, the modeling process and design methodology of control parameters are presented. In Sections V and VI, simulation and experimental results are respectively provided to verify the effectiveness of the proposed method. Finally, concluding remarks are given in Section VII.

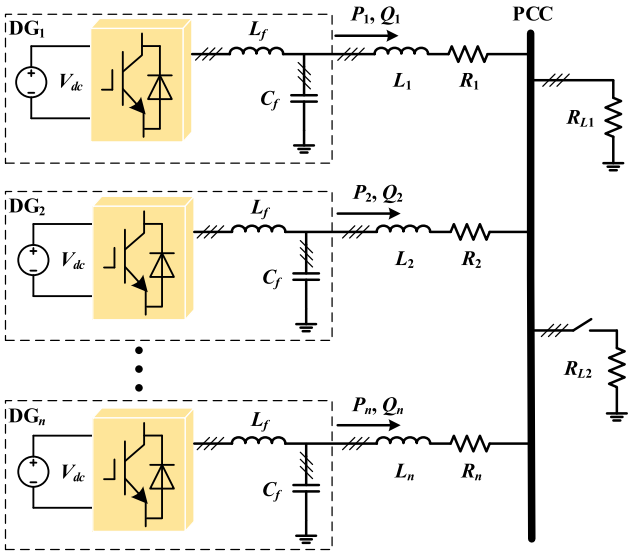

Fig. 1. Simplified system configuration of an islanded microgrid.

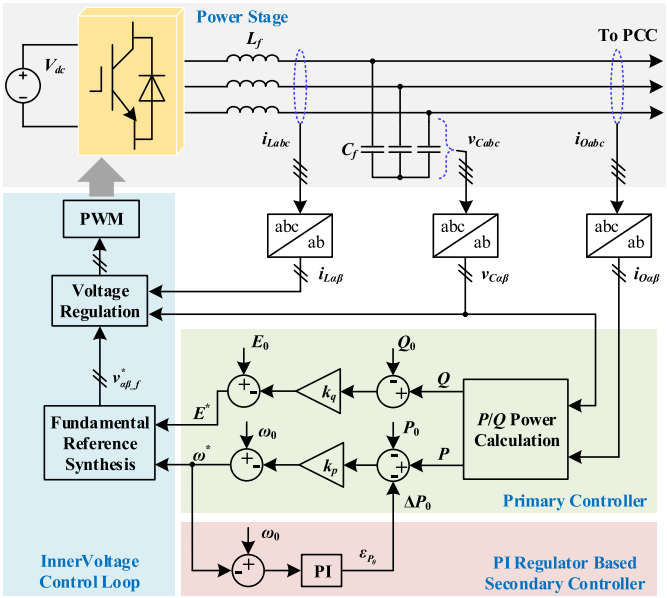

Fig. 2. Diagram of a DG equipped with primary droop control and the existing PI-SFC method.

II. Review of Primary Droop Control and PI-SFC

An islanded microgrid can be simplified as the system displayed in Fig. 1. Each DG consists of a dc link, a three-phase inverter, and a typical inductor-capacitor (*LC*) filter. The dc link voltage is assumed to be constant under regulation of a front-end power electronics converter. Then, the dc link voltage is converted into ac voltage by the inverter and the *LC* filter. The DGs are connected to the PCC through power transmission lines and supply the load collectively. In Fig. 2, the internal control structure of the DG is illustrated in detail with primary and secondary controllers. At the primary control level, the conventional P-ω and Q-E droop control method is implemented to share the load power among DGs without the help of communication links. The secondary controller is based on the PI-SFC. The operation principle and limitations of primary and secondary controllers are briefly reviewed below.

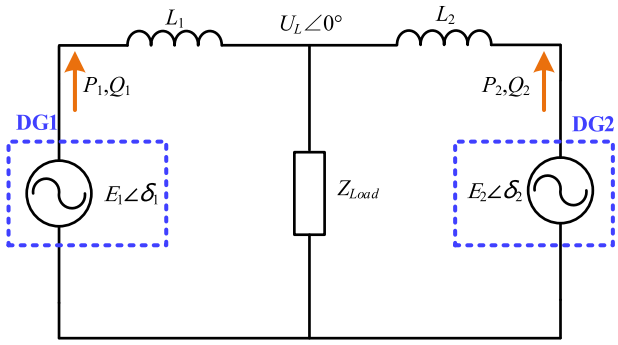

Fig. 3. Equivalent circuit of a two-DG-parallel islanded microgrid at fundamental frequency.

A. Primary Droop Control

Primary droop control is employed to realize power sharing and to synchronize each inverter, which can be mathematically expressed as follows:

$$\omega^* = \omega_0 - k_p(P - P_0) \tag{1}$$

$$E^* = E_0 - k_q(Q - Q_0) \tag{2}$$

where ω^* and E^* are the generated reference of frequency and voltage amplitude, respectively; P and Q are the output real power and reactive power, respectively, which can be calculated by (12) and (13) in a digital controller; P_0 and Q_0 are the nominal real and reactive power, respectively; ω_0 and E_0 are the nominal frequency and voltage amplitude, respectively; and k_p and k_q are respective droop gains, which are defined as positive.

An inverter under droop control can be represented by a controlled voltage source as depicted in Fig. 3, whose frequency and amplitude are regulated according to the output real and reactive power. According to the electric circuit theory, the output real and reactive power of each DG are determined by (3) and (4) under inductive feeder impedance conditions [3], [8]:

$$P = \frac{EU_L \sin\delta}{X} \tag{3}$$

$$Q = \frac{E\left(E - U_L\cos\delta\right)}{X} \tag{4}$$

where X is the reactance of the feeder inductor and δ is the phase-angle difference between terminal voltage E and PCC voltage U_L. Typically, δ is assumed to be quite small; by substituting $\sin\delta \approx \delta$ and $\cos\delta \approx 1$, (3) and (4) can be simplified as

$$P = \frac{EU_L\delta}{X} \tag{5}$$

$$Q = \frac{E\left(E - U_L\right)}{X} \tag{6}$$

based on which, one can conclude that P increases with phase-angle difference and Q increases with voltage amplitude.

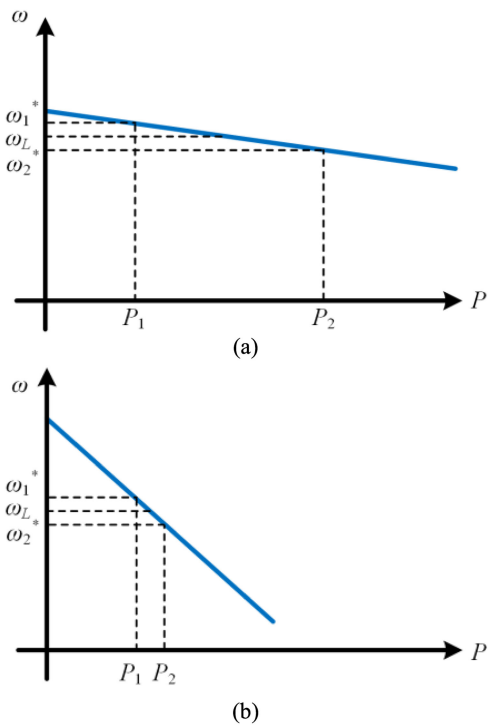

Fig. 4. Steady-state operating points of two DGs under (a) small droop gain and (b) large droop gain. ω_L is the actual system frequency; ω_1^* and ω_2^* are the reference frequency of DG_1 and DG_2; and P_1 and P_2 are the real power output by DG_1 and DG_2, respectively.

The basic operating principle of droop control can be explained by a two-DG system. Assuming that DG_1 outputs more real power than DG_2 due to disturbance, then the frequency of DG_1 will be lower than that of DG_2 according to (1), leading to a reduction in δ_1 and an increase in δ_2. The output real power P_1 will then decline and P_2 will increase based on (5). This pattern forms a self-regulating feedback mechanism to share the real power. Eventually, all DGs synchronize and reach a common frequency in a steady state; *P*-ω droop control can therefore always achieve real power sharing. The proposed SACS-SFC also utilizes this characteristic of frequency droop, which will be introduced in Section III.

As mentioned earlier, droop control has an advantage of realizing power sharing without communication links. However, primary droop control suffers from an inherent tradeoff between power-sharing accuracy and the voltage regulation rate, as explained below. In a practical microgrid, each DG operates with its own digital processor driven by the local clock, which may drift from each other [34]. In this case, the operating frequency is the same in all DGs at steady state, but different from the reference values due to the clock drift. The steady-state operating points are indicated in Fig. 4 (assuming that DG_1 and DG_2 have the same power rating for a more effective illustration), where ω_L is the actual system frequency; ω_1^* and ω_2^* are the reference frequency of DG_1 and DG_2, respectively; and P_1 and P_2 are the real power output by DG_1 and DG_2, respectively. Obviously, if the droop gains are designed to be small as in Fig. 4(a), the frequency deviation resulting from load variation is slight, but a very small clock drift can lead to significant real power sharing error. Conversely, if the droop gains are designed to be larger as in Fig. 4(b), the output power difference between DGs can be reduced, whereas larger frequency deviations will arise when the load power demand changes. To ensure adequate power sharing and fast response of the microgrid, droop gains tend to be larger. Accordingly, secondary control must be adopted for frequency restoration.

B. Principle of PI-SFC and Its Limitation

The secondary control concept is thought to compensate for frequency and voltage deviation. To fully restore frequency and avoid dependence on MGCC or communication links among DGs, the PI-SFC was implemented in the local controller of each DG in [27] and [28]. The frequency of output voltage can be compared with the nominal frequency, and the difference between them is compensated to zero by a PI regulator. Meanwhile, the output of the PI regulator tunes nominal real power in the primary droop controller in real time to adjust the frequency. The overall control block diagram is illustrated in Fig. 2, where ω_0 is the nominal frequency and ω^* is the frequency reference generated by the primary droop controller. Note that the frequency reference, rather than the actual frequency, is selected as the feedback value for the secondary controller. This is because the bandwidth of the inner voltage loop is much greater than that of the droop control loop; as such, the actual frequency tracks the reference value perfectly [35], [36]. Therefore, measuring output voltage frequency is saved. The secondary controller generates a compensation signal ΔP_0, which is added into the primary *P*-ω droop control to regulate the nominal real power P_0 as follows:

$$\omega^* = \omega_0 - k_p \left(P - P_0 - \Delta P_0\right). \tag{7}$$

The compensation value of nominal real power equals the output of the secondary PI regulator expressed as

$$\Delta P_0 = \varepsilon_{P_0} \tag{8}$$

$$\varepsilon_{P_0} = \left(k_{p\omega} + \frac{k_{i\omega}}{s}\right)(\omega_0 - \omega^*) \tag{9}$$

where ε_{P_0} is the output of the PI regulator and $k_{p\omega}$ and $k_{i\omega}$ are the proportional and integral gains, respectively.

The PI-SFC can restore frequency fully; however, real power sharing may deteriorate during the frequency restoration process as explained below. To ensure real power sharing, the nominal real power (P_0) and its compensation value (ΔP_0) of each DG should always be kept identical. However, ΔP_0 (i.e., the output of the PI regulator) in each DG is closely related to its own integration history, which is highly likely to differ across DGs due to various factors, e.g., computational inaccuracies, measurement system, and nonhomogeneous delays. To further complicate matters, this difference in ΔP_0 may be accumulated over time by the integrator due to a lack of MGCC or communication links. Therefore, real power sharing declines gradually. To demonstrate the aforementioned limitation of the PI-SFC, the integration difference is emulated and accelerated by starting the secondary controller at different moments for different

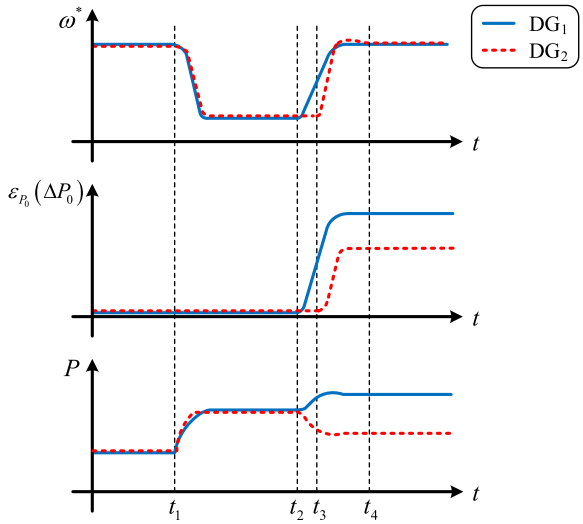

Fig. 5. Sketchy waveforms of frequency reference ω^*, the output value of PI regulator ε_{P_0} (or nominal real power compensation value ΔP_0), and the output real power P of two DGs during the frequency restoration process of PI-SFC.

DGs in the subsequent analysis, simulations, and experiments. Fig. 5 shows the sketchy waveforms of the frequency reference, nominal real power compensation value, and real power of two DGs during a load change and frequency restoration process. Initially, only conventional droop control is applied; the fundamental frequency thus drops at $t = t_1$ due to a load increase. To demonstrate the cause of unequal real power sharing, the two DGs are assumed to initiate secondary regulation at $t = t_2$ and $t = t_3$, respectively. This difference in the starting moment emulates the unique integration process in each DG in a real microgrid. Then, different compensation values of nominal real power can be observed, suggesting that the droop curves of DG_1 and DG_2 shift to different positions due to distinct output from the secondary controller. Finally, a significant real power-sharing error is produced. Therefore, even though the PI regulator can restore frequency to the nominal value, the P-ω droop characteristic of each DG will be shifted differently by the PI regulator, causing real power sharing to deteriorate, as illustrated in Fig. 6(a). This is the major limitation of PI-SFC.

To achieve sound real power-sharing performance during secondary frequency restoration, as shown in Fig. 6(b), while regulating frequency in a decentralized manner, a communicationless secondary frequency restoration control method based on the SACS injection is proposed in this article.

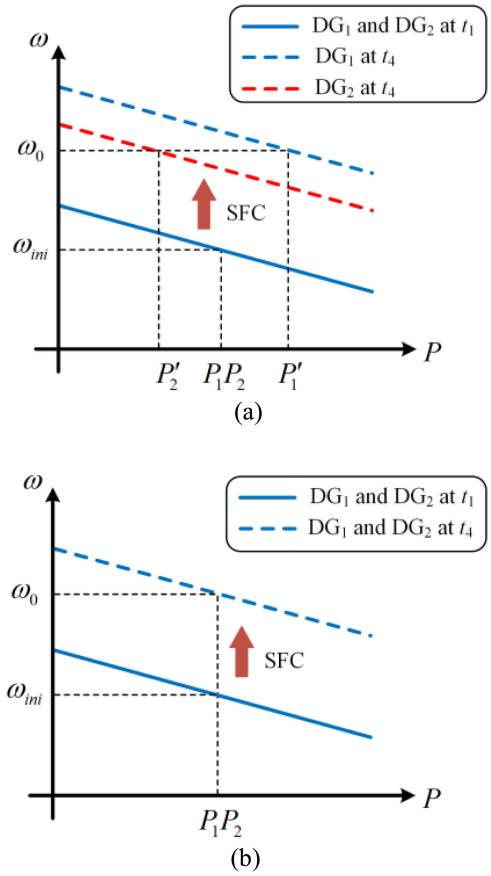

Fig. 6. Steady-state operating points of two DGs during frequency restoration by (a) the PI-SFC method, and (b) the expected ideal secondary frequency controller.

III. Proposed SACS-Injection-Based SFC Method

A. Description of Overall Control Method

The overall control block diagram of the proposed SACS-SFC is illustrated in Fig. 7. The primary droop controller is identical to that in the PI-SFC. Major improvements pertain to the secondary control level and inner voltage control loop, which are highlighted within the red dashed line box.

In the inner voltage control loop, a SACS reference voltage, which has constant amplitude and variable frequency, is included in the total reference voltage. A corresponding voltage resonant controller is simultaneously employed to ensure that the output voltage can track the reference precisely. Therefore, the output voltage of each DG contains the SACS component and leads to SACS power flowing among all DGs. At the secondary control level, the compensation value of nominal real power (ΔP_0) is synthesized by the output of the PI regulator and the real power produced by the SACS as follows:

$$\begin{aligned}\Delta P_0 &= \varepsilon_{P_0} + G_p P_{\rm ss} \\ &= \left(k_{p\omega} + \frac{k_{i\omega}}{s}\right)(\omega_0 - \omega^*) + G_p P_{\rm ss} \end{aligned} \tag{10}$$

where $P_{\rm ss}$ is the real power generated by the SACS and G_p is a constant coefficient labeled amplification gain. Because the SACS real power is too small to regulate ΔP_0, G_p is used to amplify the effect of the SACS. Moreover, the compensation value ΔP_0 is used to regulate the SACS frequency given the following droop relation:

$$\omega_{\rm ss}^* = \omega_{\rm ss0} - k_{\rm ss}\Delta P_0 \tag{11}$$

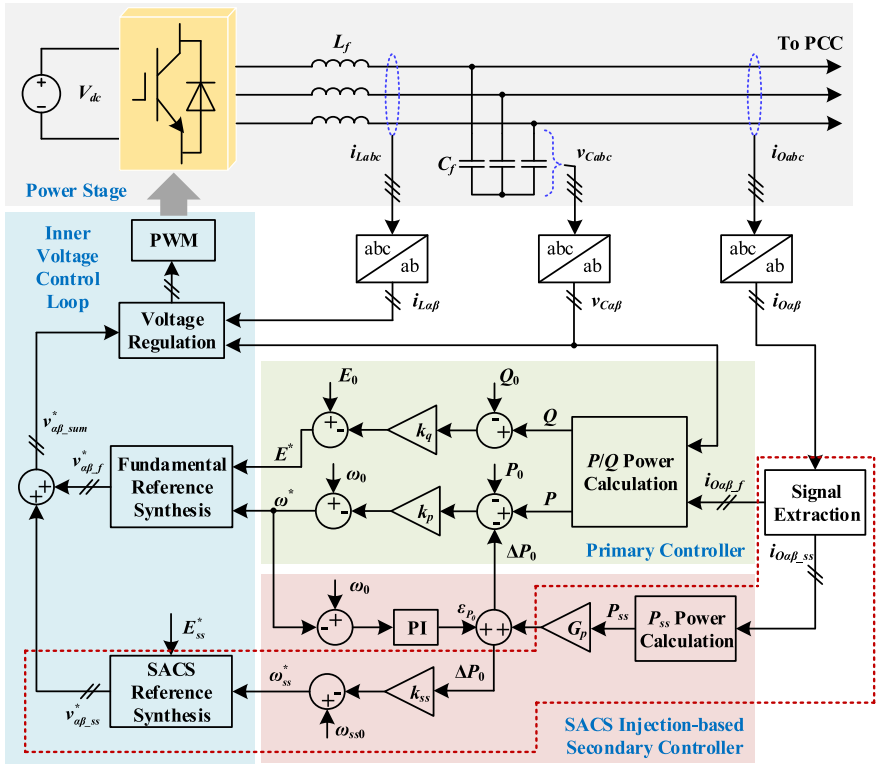

Fig. 7. Diagram of a DG equipped with the proposed SACS-SFC, where elements inside the dashed box are added compared to PI-SFC.

where $\omega_{\rm ss}^*$ is the generated SACS frequency reference, $\omega_{\rm ss0}$ is the nominal SACS frequency, and $k_{\rm ss}$ is the SACS frequency droop gain, which is defined as positive. The designs of SACS amplitude and nominal frequency are introduced comprehensively in Section IV-A.

To obtain the exact values of fundamental power and SACS real power, a signal extraction block is employed to separate the SACS current from the fundamental current. Then, the fundamental real power, reactive power, and SACS real power can be calculated as follows:

$$P = \frac{3}{2}\frac{\omega_{cp}}{s+\omega_{cp}}\left(v_{C\alpha}i_{O\alpha\_f} + v_{C\beta}i_{O\beta\_f}\right) \tag{12}$$

$$Q = \frac{3}{2}\frac{\omega_{cp}}{s+\omega_{cp}}\left(v_{C\beta}i_{O\alpha\_f} - v_{C\alpha}i_{O\beta\_f}\right) \tag{13}$$

$$P_{\rm ss} = \frac{3}{2}\frac{\omega_{cp}}{s+\omega_{cp}}\left(v_{\alpha\_\rm ss}^*i_{O\alpha\_\rm ss} + v_{\beta\_\rm ss}^*i_{O\beta\_\rm ss}\right) \tag{14}$$

where $v_{C\alpha}$ and $v_{C\beta}$ represent the α- and β-axis components of the capacitor voltage, respectively; $i_{O\alpha\_f}$ and $i_{O\beta\_f}$ are, respectively, the α- and β-axis components of the extracted fundamental current; $i_{O\alpha\_\rm ss}$ and $i_{O\beta\_\rm ss}$ are, respectively, the α- and β-axis components of the extracted SACS current; $v_{\alpha\_\rm ss}^*$ and $v_{\beta\_\rm ss}^*$ are, respectively, the α- and β-axis components of the SACS reference voltage; and ω_{cp} is the cutoff frequency for LPFs, which are used to attenuate ripples in the calculated powers. The cutoff frequency for LPFs is set very low to achieve effective ripple attenuation and avoid interaction with the inner voltage regulation loop [35], [36]. In this article, the LPF cutoff frequency is set to 5 Hz. Note that the reference voltage rather than the actual SACS output voltage is used to calculate $P_{\rm ss}$. This approximation saves signal extraction of the SACS voltage without introducing significant calculation errors.

B. Operation Principle

The distinctive feature of the proposed secondary frequency controller is that the compensation value of nominal real power ΔP_0 is regulated simultaneously by the PI regulator and the SACS real power. Similar to PI-SFC, the PI regulator in the proposed method is still responsible for frequency restoration, which represents the major function of the secondary control level. Further, the SACS is injected to avoid the real power-sharing issue following from integration, which is realized by establishing a droop relation between ΔP_0 and the SACS frequency. This proposed SACS droop controller can regulate ΔP_0 of each DG into an identical value, thereby ensuring real power sharing.

Similar to the P-ω droop control, all parallel-connected DGs produce the same SACS frequency when synchronized in a steady state, which further ensures an identical value of ΔP_0 for each DG according to droop relation (11). In terms of the primary droop controller of the fundamental voltage, an identical ΔP_0 will lead each DG to output an even amount of real power. The regulation process is briefly shown in Fig. 8, where the fundamental frequency drops at $t = t_1$ because of a

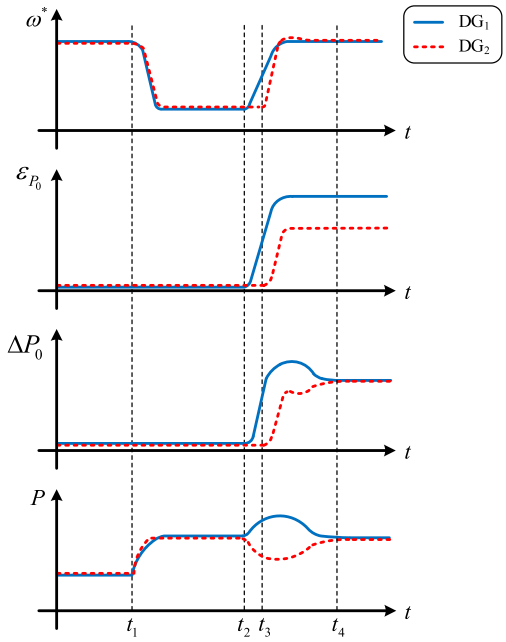

Fig. 8. Sketchy waveforms of frequency reference ω^*, output of PI regulator ε_{P_0}, nominal real power compensation value ΔP_0, and output real power P of two DGs during the frequency restoration process of the proposed SACS-SFC.

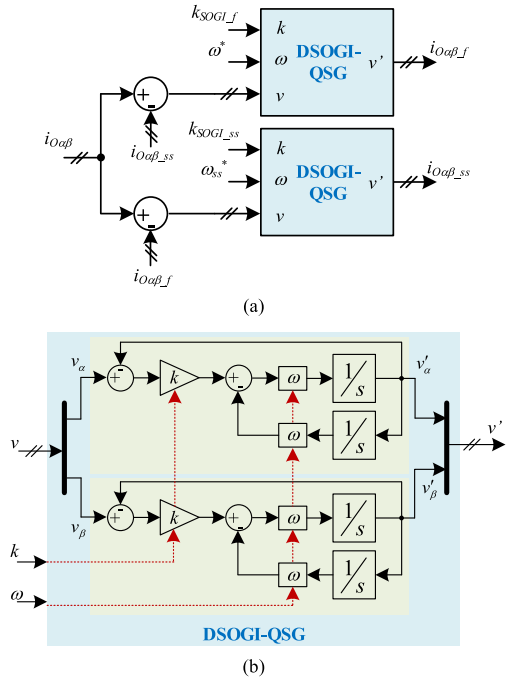

Fig. 9. Block diagram of (a) SOGI-based current signal extraction used in the proposed method and (b) DSOGI-QSG [40].

load increase and the two DGs initiate frequency restoration at $t = t_2$ and $t = t_3$, respectively. The frequency is restored and the output of PI regulator differs due to different starting moments of secondary regulation. Yet despite these differences, the compensation value ΔP_0 is regulated to be identical for both DGs using the proposed SACS droop controller, leading to even real power sharing between DGs.

To conclude, under the proposed SACS-SFC method, the fundamental frequency can be restored to the nominal value by the PI frequency regulator while accurate real power sharing can be maintained by the SACS droop controller.

C. Current Signal Extraction

To precisely calculate the fundamental power and SACS real power, a signal extraction method based on a second-order generalized integrator (SOGI) is used to separate the SACS current from the fundamental current [37], [41]. A block diagram of current signal extraction is presented in Fig. 9(a), which consists of two dual SOGI quadrature signal generators (DSOGI-QSGs). Each DSOGI-QSG contains two SOGI-QSGs that operate on the α-axis and β-axis, respectively, as shown in Fig. 9(b). The transfer function of each SOGI-QSG from the input signal v to the output signal v' is shown as

$$D(s) = \frac{v'}{v}(s) = \frac{k\omega s}{s^2 + k\omega s + \omega^2}. \tag{15}$$

The SOGI-QSG behaves as a band-pass filter, which only allows a signal at the resonant frequency ω to pass. The gain k in (15) determines the bandwidth of the SOGI-QSG, which is set to $\sqrt{2}$ according to [41]. The upper DSOGI-QSG in Fig. 9(a), with resonant frequency ω^*, is intended to extract the fundamental current component $i_{O\alpha\_f}$. Meanwhile, the lower DSOGI-QSG with resonant frequency $\omega_{\rm ss}^*$ is intended to extract the SACS current component $i_{O\alpha\_\rm ss}$.

D. Reference Voltage Synthesis and Tracking

As depicted in Fig. 7, the total reference voltage is synthesized by the fundamental reference voltage and SACS reference voltage. With the fundamental frequency reference and amplitude reference generated by the primary droop controller, the fundamental reference voltage can be expressed in $\alpha\beta$ frame as follows:

$$v_{\alpha\_f}^* = E^* \cos\left(\int \omega^* dt\right) \tag{16a}$$

$$v_{\beta\_f}^* = E^* \sin\left(\int \omega^* dt\right) \tag{16b}$$

where $v_{\alpha\_f}^*$ and $v_{\beta\_f}^*$, respectively, denote the α- and β-axis components of the fundamental reference voltage. Moreover, with the SACS frequency reference derived in (11) and a constant amplitude $E_{\rm ss}^*$, the SACS reference voltage can be expressed in $\alpha\beta$ frame as follows:

$$v_{\alpha\_\rm ss}^* = E_{\rm ss}^* \cos\left(\int \omega_{\rm ss}^* dt\right) \tag{17a}$$

$$v_{\beta\_\rm ss}^* = E_{\rm ss}^* \sin\left(\int \omega_{\rm ss}^* dt\right) \tag{17b}$$

where $v_{\alpha\_\rm ss}^*$ and $v_{\beta\_\rm ss}^*$ are the α- and β-axis components of the SACS reference voltage, respectively. Therefore, the overall

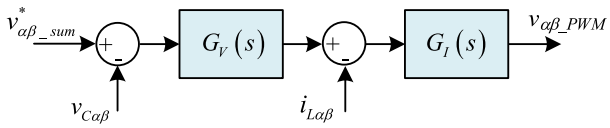

Fig. 10. Block diagram of voltage regulation in the proposed control method.

reference voltage can be obtained by summing the fundamental and SACS reference voltage

$$v^*_{\alpha\_\mathrm{sum}} = v^*_{\alpha\_f} + v^*_{\alpha\_\mathrm{ss}} \tag{18a}$$

$$v^*_{\beta\_\mathrm{sum}} = v^*_{\beta\_f} + v^*_{\beta\_\mathrm{ss}} \tag{18b}$$

where $v^*_{\alpha\_\mathrm{sum}}$ and $v^*_{\beta\_\mathrm{sum}}$ refer to the α- and β-axis components of the total reference voltage, respectively.

To achieve excellent reference voltage tracking, a dual-loop voltage regulation structure is adopted, as shown in Fig. 10. The outer loop is an *LC* filter capacitor voltage control loop with a proportional resonant (PR) controller, and the inner loop is an inductor current control loop with a proportional controller [37]. The voltage regulators for the dual-loop structure are expressed as follows:

$$G_V(s) = k_{pV} + \frac{2k_{if}\omega_c s}{s^2 + 2\omega_c s + (\omega^*)^2} + \frac{2k_{\mathrm{iss}}\omega_c s}{s^2 + 2\omega_c s + (\omega^*_{\mathrm{ss}})^2} \tag{19}$$

$$G_I(s) = k_{pI} \tag{20}$$

where $G_V(s)$ and $G_I(s)$ are the transfer functions of the voltage regulator and current regulator, respectively; k_{pV} is the gain of the voltage proportional controller; k_{if} and k_{iss} are the gains of the fundamental and SACS resonant controllers, respectively; ω_c is the cutoff frequency of the resonant controllers; and k_{pI} is the gain of the current proportional controller. As indicated in (19), an independent resonant controller whose resonant frequency is set at the SACS frequency is applied to guarantee excellent tracking of the SACS reference voltage. Moreover, as frequencies are determined by the droop equations in (1) and (11), and may deviate from their rated values, the proposed PR controllers should adaptively adjust their resonant frequencies. Note that the proportional controller in the inner current control loop is used to increase internal stability.

IV. Modeling and Parameter Design

In the proposed SACS-SFC, the frequency and amplitude of the injected SACS must be selected carefully. Moreover, the control parameters associated with secondary control, i.e., SACS droop gain k_{ss}, amplification gain G_p, and PI gains, are discussed at length in this section. The amplification gain is designed based on the steady-state analysis; the droop gain and PI gains are designed based on a dynamic system model. The model for conventional droop control, including primary control and the inner voltage control loop, has been already well established in the literature [35], [36]. Thus, the model built in this article only considers the effect of secondary control, namely the injected SACS and frequency restoration process. To simplify the discussion, a system with two DGs in a similar topology as Fig. 1 is analyzed in this section.

A. SACS Frequency and Amplitude Design

The SACS plays an important role in the proposed method. To avoid introducing excessive effects into the system, the frequency and amplitude of the injected SACS must be designed carefully.

1) Design of SACS Frequency: The frequency of the injected SACS is roughly $\omega_{\mathrm{ss}0}$ and drifts slightly according to ΔP_0, as shown in (11). Hence, the design of the rated frequency $\omega_{\mathrm{ss}0}$ is important. To guarantee that the injected signal is well controlled and can be easily extracted without deteriorating the output voltage quality, the following criteria should be met when selecting the SACS frequency.

First, the SACS current must be extracted from the output current; however, the accuracy of signal extraction could be affected by preexisting system harmonics. Thus, the main preexisting system harmonics should be recognized in advance so as not to be selected as the SACS frequency. Low-order odd harmonics can often occur in the system due to nonlinear loads or modulation [38]. Therefore, a frequency of odd multiples of the fundamental frequency is not recommended for the SACS. Second, a frequency of interharmonics or subharmonics is likewise not recommended for the SACS, because the limit for each in an electrical system tends to be more rigorous [39]. Third, the SACS frequency cannot be set too high because a high frequency will exceed the control loop bandwidth or be suppressed by the output *LC* filter. Last but not the least, to accurately separate the fundamental signal and SACS, the SACS frequency cannot be set too close to the fundamental frequency. Accordingly, in this article, $\omega_{\mathrm{ss}0}$ is set to four times the fundamental frequency ($2\pi*200$ rad/s) as an example.

2) Design of SACS Amplitude: Regarding the selection of SACS amplitude, it is a small constant value that should be designed with a focus on the tradeoff between signal extraction and the power quality limitation. On the one hand, signals with large amplitudes can ease signal extraction. Yet power quality standards, such as in [39], limit the total harmonic distortion (THD) in voltage within 8% and individual harmonics within 5%. On the other hand, the minimum amplitude is limited by the resolution of analog-to-digital converter, signal extraction algorithm, and signal-to-noise ratio. Based on the experience, the SACS amplitude can be set to 0.5–2% of the fundamental voltage amplitude, which will not exceed the THD limitations and can be extracted successfully.

B. Steady-State Analysis and Design of Amplification Gain

The steady-state operating point of the proposed method is analyzed here to design a proper value for G_p. When the system reaches a steady state, the SACS frequency in each DG synchronizes to a common value, and ΔP_0 is identical for each DG according to (11); in other words, $\omega_{\mathrm{ss}1} = \omega_{\mathrm{ss}2}$ and

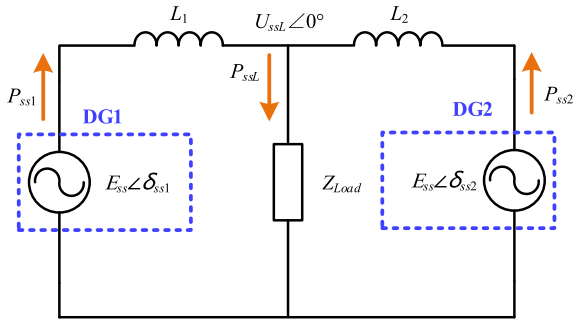

Fig. 11. Equivalent circuit of a two-DG-parallel islanded microgrid presenting components at the frequency of the injected SACS.

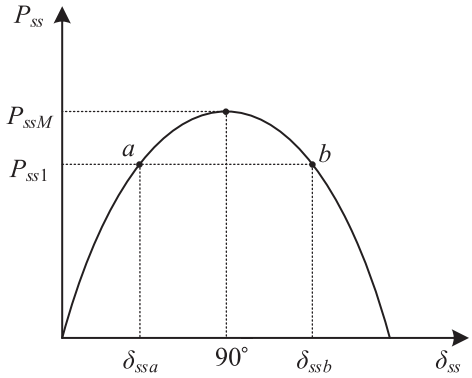

Fig. 12. Variation of real power with phase angle in each DG unit at the frequency of the injected SACS.

$\Delta P_{01} = \Delta P_{02}$. The following equation can thus be derived:

$$\varepsilon_{P_{01}} + G_p P_{\mathrm{ss1}} = \varepsilon_{P2} + G_p P_{\mathrm{ss2}}. \tag{21}$$

Then, the difference in SACS real power between DG_1 and DG_2 can be obtained

$$P_{\mathrm{ss1}} - P_{\mathrm{ss2}} = \frac{\varepsilon_{P_{02}} - \varepsilon_{P_{01}}}{G_p}. \tag{22}$$

The real power produced by the SACS of each DG demonstrates the following relationship:

$$P_{\mathrm{ss1}} + P_{\mathrm{ss2}} = P_{\mathrm{ss}L} \tag{23}$$

where $P_{\mathrm{ss}L}$ is the SACS real power absorbed by the load. $P_{\mathrm{ss}L}$ can be regarded as a constant value if the load does not change. Based on (22) and (23), the SACS real power of each DG in a steady state can be calculated as

$$P_{\mathrm{ss1}} = \frac{P_{\mathrm{ss}L}}{2} + \frac{\varepsilon_{P_{02}} - \varepsilon_{P_{01}}}{2G_p} \tag{24a}$$

$$P_{\mathrm{ss2}} = \frac{P_{\mathrm{ss}L}}{2} - \frac{\varepsilon_{P_{02}} - \varepsilon_{P_{01}}}{2G_p}. \tag{24b}$$

The SACS real power in steady state is related to the amplification gain and the output difference of the PI regulators. To ensure system stability, G_p needs to be designed carefully so the SACS real power can be limited to a reasonable range.

Similar to the equivalent circuit at the fundamental frequency in Fig. 3, the equivalent circuit at the SACS frequency can be derived, as shown in Fig. 11. Taking DG_1 as an example, the output SACS real power of DG_1 can be expressed as follows:

$$P_{\mathrm{ss1}} = \frac{E_{\mathrm{ss}} U_{\mathrm{ss}L}}{X_{\mathrm{ss1}}} \sin\delta_{\mathrm{ss1}} \tag{25}$$

where $U_{\mathrm{ss}L}$ represents the SACS voltage at the PCC and δ_{ss1} is the phase angle of DG_1. The variation of SACS real power with the phase angle is depicted in Fig. 12. The real power varies as a sinusoidal wave of the angle, exhibiting a highly nonlinear relationship. When the angle is smaller than 90°, e.g., point a, the real power increases along with the angle; however, a further increase in the angle results in a reduction in power when the angle exceeds 90°, e.g., point b. According to the power angle stability criteria in the power system, a necessary condition for ensuring that all DGs remain in synchronism and operate stably is to keep the angle below 90° [42]. To evaluate the degree of angle stability, the stability reservation coefficient K_P is defined as follows:

$$K_P = \frac{P_{\mathrm{ss}M} - P_{\mathrm{ss1}}}{P_{\mathrm{ss1}}} \times 100\% \tag{26}$$

where $P_{\mathrm{ss}M}$ is the maximum transferred power when δ_{ss} equals 90°. An increase in K_P results in a larger angle stability margin, whereas the transferred power will decline. In power system design guides such as [43], K_P is recommended to be at least 20% to retain a sufficient stability margin. However, different from a power system, the principal function of the SACS is to establish a link among DGs instead of transferring power; therefore, K_P can be designed to be larger than in a power system to guarantee a sufficient stability margin. Based on this phenomenon, a K_P larger than 40% is recommended in this control method. The upper limit for SACS real power can be obtained

$$P_{\mathrm{ss1}} \le \frac{P_{\mathrm{ss}M}}{1.4}. \tag{27}$$

By substituting (24a) into (27), the minimum value for amplification gain G_p can be determined as follows:

$$G_p \ge \frac{0.7 X_{\mathrm{ss1}} \left(\varepsilon_{P_{02}} - \varepsilon_{P_{01}}\right)}{E_{\mathrm{ss}} U_{\mathrm{ss}L} - 0.7 X_{\mathrm{ss1}} P_{\mathrm{ss}L}}. \tag{28}$$

To simplify this calculation, $U_{\mathrm{ss}L}$ can be assumed to be equal to E_{ss}. The output difference of the PI regulator, i.e., $\varepsilon_{P_{02}} - \varepsilon_{P_{01}}$, is related to the integration process and is therefore not a constant value. However, its maximum value can be predicted, where the output of the PI regulator in DG_2 reaches its upper limit and DG_1 reaches its lower limit. Therefore, the minimum value for G_p can be determined under this circumstance. Conversely, if G_p is too large, then the circulating SACS real power between DGs will be exceedingly small, which may hinder the SACS regulation in some highly distributed systems. Therefore, designing G_p to be equal to its minimum value, as in (28), is preferred.

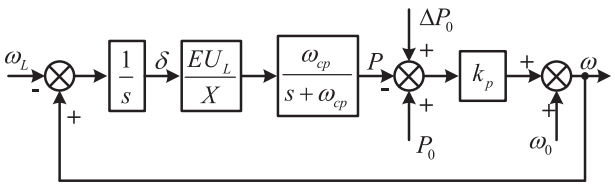

Fig. 13. Dynamic model of primary droop control, where ω_L represents the PCC frequency.

C. Dynamic System Model and Design of SACS Droop Gain and PI Gains

In this section, a dynamic model considering the proposed secondary control is built to analyze the system stability and to derive the parameter design methodology for $k_{\rm ss}$ and PI gains. Because the bandwidth of the inner voltage control loop is much greater than that of the proposed secondary control, the dynamic response of the voltage regulation is ignored here.

To guarantee system stability, the control bandwidth must be reduced with an increase in the control level; that is, the secondary control level should be designed to be much slower than the primary control level [6], [20], [44]. Thus, the bandwidth of the primary droop control should be designed first, based on which the bandwidth of the secondary control can be determined. The dynamic model for primary droop control is illustrated in Fig. 13, where ω_L represents the PCC voltage frequency. The primary control loop ensures synchronization of each DG and, thus, realizes real power sharing. As the dynamic response of the secondary control is much slower than the primary control, the compensation value of nominal real power (ΔP_0) is regarded as a constant when analyzing the primary control. The closed loop transfer function of the primary control is

$$G_d(s) = \frac{\omega}{\omega_L} = \frac{k_p s\left(s+\omega_{cp}\right)}{s^2+\omega_{cp}s+\frac{k_p E U_L \omega_{cp}}{X}}. \tag{29}$$

The bandwidth of the primary control can be obtained accordingly, which is related to the droop gain k_p. Because the design of k_p is beyond the scope of this article, k_p is designed according to [3] and [6] as follows:

$$k_p = \frac{2P_0}{\omega_{\max}-\omega_{\min}} \tag{30}$$

where $\omega_{\max}$ and $\omega_{\min}$ denote the allowed maximum and minimum frequency, respectively.

Once the bandwidth of the primary control has been determined, the bandwidth of the secondary control can be selected to be 1/10–1/5 of the primary control according to the experience. The dynamic model for the proposed secondary control is shown in Fig. 14. When assessing the dynamic response of the secondary control, the primary control can be assumed to operate in a steady state, represented by the steady-state relationship in (7). The dynamic model for the proposed secondary control has a distinctive feature wherein ΔP_0 is determined by the PI control loop and SACS control loop concurrently. The PI control loop is responsible for restoring system frequency, while the SACS control loop is responsible for trimming ΔP_0 of each DG to be equal. To avoid interference of these two control loops and to simplify evaluation, their bandwidths are deliberately separated. The PI control loop and SACS control loop can then be analyzed independently. There are two options: designing the PI control loop to be faster than the SACS control loop, or designing the SACS control loop to be faster than the PI control loop. Both options are feasible, but the control effects differ. If the PI control loop is designed to be faster than the SACS control loop, frequency restoration can be very fast, but transient real power-sharing errors may manifest in the dynamic process. On the contrary, if the SACS control loop is designed to be faster than the PI control loop, then power sharing can be ensured, but frequency restoration requires longer time. Considering that frequency deviation is more deleterious than the power-sharing issue for the power system in most cases [45], the PI control loop is designed to be faster than the SACS control loop in this article.

When the bandwidth of the PI control loop is designed to be 5–10 times larger than the SACS control loop, interference between these control loops can be ignored. Their corresponding closed loop transfer function can then be obtained as

$$G_{\rm PI}(s) = \frac{\omega}{\omega_0} = \frac{k_p\left(k_{p\omega}s+k_{i\omega}\right)}{s} \tag{31}$$

$$G_{\rm SACS}(s) = \frac{\omega_{\rm ss}}{\omega_{{\rm ss}L}} = \frac{s\left(s+\omega_{cp}\right)}{s^2+\omega_{cp}s+\frac{k_{\rm ss}E_{\rm ss}U_{{\rm ss}L}\omega_{cp}G_p}{X_{\rm ss}}}. \tag{32}$$

It can be seen that the bandwidth of the PI control loop is determined by PI gains, and that of the SACS control loop is determined by droop gain $k_{\rm ss}$. Based on the models in (29), (31), and (32) and bandwidth limitations given by [6], [20], [44], all control parameters can be designed through the following steps.

1) Design the primary droop gain k_p according to (30), after which the bandwidth of the primary control can be obtained according to (29).
2) Once the bandwidth of primary control is determined, the bandwidth of PI control loop can be set to 1/10–1/5 of it, based on which the cross frequency can be limited in a certain range. Note that the PI control loop in (31) is a simple first-order system, one can use the SISO tool in MATLAB to design the optimum proportional gain and integral gain considering both dynamic response and high-frequency disturbance suppression.
3) According to the model in (32), the bandwidth of SACS control loop is related with $k_{\rm ss}$ and G_p. Since G_p has already been determined in the previous section, the range of $k_{\rm ss}$ can be easily designed to ensure that the bandwidth of the SACS control loop is about 1/10–1/5 of the PI control loop.

Following the aforementioned steps, the bode diagrams and step response of the primary control loop, PI control loop, and SACS control loop are shown in Figs. 15 and 16. The bandwidths of these three control loops are distinct and the dynamic response speed is proportional to the bandwidth. Therefore, all control parameters can be designed and system stability can

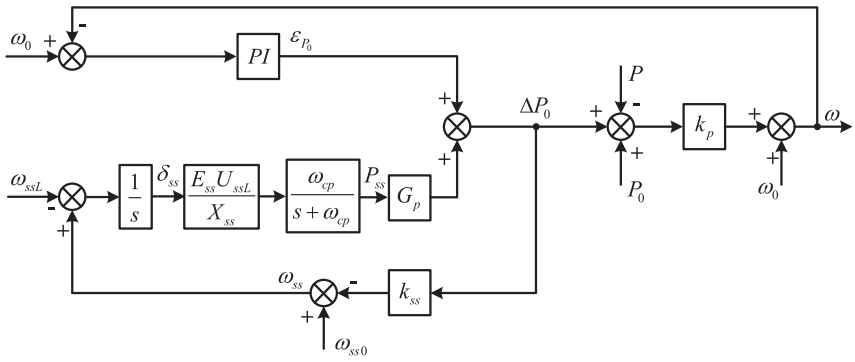

Fig. 14. Dynamic system model of the proposed SACS-SFC method.

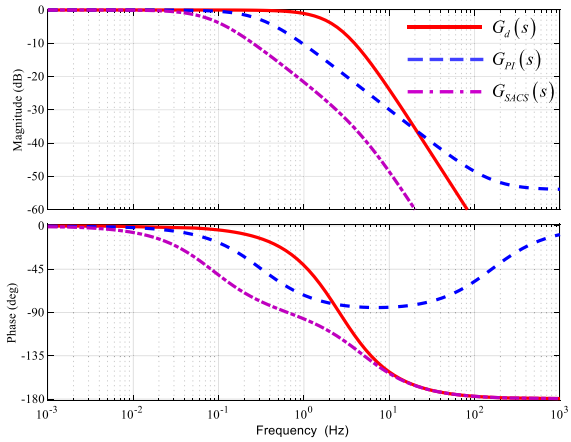

Fig. 15. Closed-loop bode diagrams of primary droop control loop $G_d(s)$, PI control loop $G_{\mathrm{PI}}(s)$, and SACS control loop $G_{\mathrm{SACS}}(s)$.

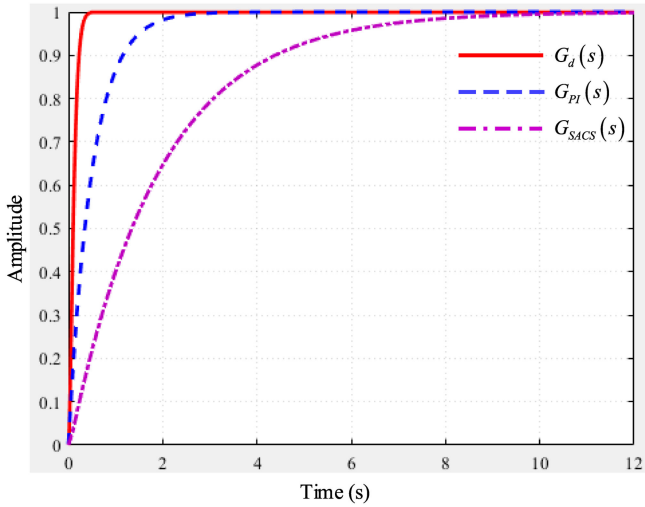

Fig. 16. Step response of primary droop control loop $G_d(s)$, PI control loop $G_{\mathrm{PI}}(s)$, and SACS control loop $G_{\mathrm{SACS}}(s)$.

be ensured. It is worth mentioning that when a microgrid is operating under heavy-load conditions, the SACS control loop should be designed to be faster than the PI control loop to ensure power sharing and avoid DG overloading during the transient.

V. Simulation Results

To verify the effectiveness of the proposed method and its parameter design methodology, simulations with two DGs connected under the same topology are shown in Fig. 1 have been conducted in PSCAD. The power stage and control system parameters are listed in Table I.

The simulation process is designed as follows. Initially, conventional droop control without secondary control is applied before 3.0 s. A resistive load power increase occurs at 2.0 s, resulting in an obvious frequency drop. Then, the secondary control for DG_1 and DG_2 is activated at 3.0 s and 3.02 s, respectively. This small time difference is used to emulate the different integration process in each DG in a real microgrid.

A. Performance Verification of the Proposed SACS-SFC

To clearly demonstrate the effectiveness of the proposed method, simulation results under the existing PI-SFC and the proposed SACS-SFC are compared in this section.

First, the PI-SFC displayed in Fig. 2 is implemented in each DG. After following the aforementioned simulation process, Fig. 17 illustrates the waveforms of output real power P, fundamental frequency f, and the compensation value of nominal real power ΔP_0 (equal to the output of PI regulator ε_{P_0} in this case) in each DG. The output of PI regulator ε_{P_0} of the two DGs differs due to the unique activation moment of secondary control. Consequently, without the help of SACS, although the frequency is drawn back to the rated value of 50.00 Hz, the real power is not shared equally between DGs. Such a phenomenon corroborates with the analysis in Section II-B.

Next, the proposed SACS-SFC method shown in Fig. 7 is implemented following the same simulation process. In this simulation, a SACS with an amplitude of 1.15 V and a nominal frequency of 200 Hz is generated by each DG. Simulation results containing output real power P, fundamental frequency f,

TABLE I
PARAMETERS OF STUDIED ISLANDED MICROGRID IN SIMULATIONS AND EXPERIMENTS

Symbol	Description	Value	
		Simulation	Experiment
V_{dc}	DC voltage (V)	600	600
f_s	Switching frequency (kHz)	12.5	12.5
S	Capacity of each DG (kVA)	N/A	9
L_f	Filter inductance (mH)	3	3
C_f	Filter capacitance (μF)	30	30
L_n+R_n	Feeder impedance of DG$_n$ (mH+Ω)	DG$_1$, 4+1; DG$_2$, 3+0.9	All DGs are about 4+1
R_{L1}	Load resistor (Ω)	10	20
R_{L2}	Load resistor (Ω)	10	10
k_p	P-ω droop gain (rad/s/W)	1.25e-3	6.25e-4
k_q	Q-E droop gain (V/var)	1.15e-4	8e-5
ω_0	Nominal fundamental frequency (rad/s)	100π	100π
E_0	Nominal fundamental voltage amplitude (V)	160	160
$k_{p\omega}$	Proportional gain	10	20
$k_{i\omega}$	Integral gain	1e4	2e4
k_{ss}	SACS droop gain (rad/s/W)	1.8e-3	1.25e-3
G_p	SACS amplification gain	5000	3000
ω_{ss0}	Nominal SACS frequency (rad/s)	400π	400π
E_{ss}^*	SACS amplitude (V)	1.15	1.15
ω_{cp}	Cutoff frequency of LPFs for power calculation (rad/s)	31	31

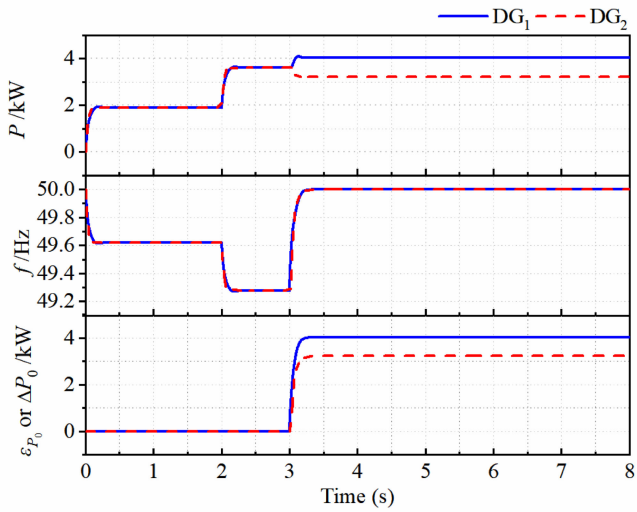

Fig. 17. Simulated waveforms of the output real power P, frequency f, and compensation value of nominal real power ΔP_0 of two DGs under existing PI-SFC.

the output of PI regulator ε_{P_0}, the compensation value of nominal real power ΔP_0, and the frequency and real power of SACS are shown in Fig. 18. The output of the PI regulator of the two DGs is still not the same due to a different activation moment of secondary control. However, the injected SACSs generate certain amounts of real power, which contribute to regulation of

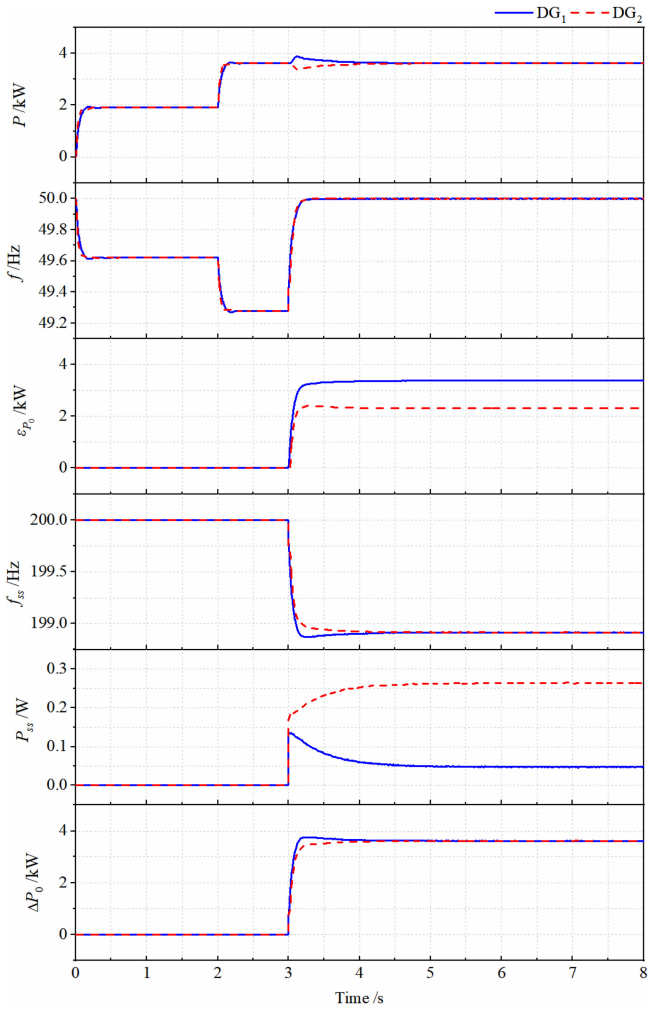

Fig. 18. Simulated waveforms of the output real power P, frequency f, output of PI regulator ε_{P_0}, SACS frequency f_{ss}, SACS real power P_{ss}, and compensation value of nominal real power ΔP_0 of two DGs under the proposed SACS-SFC.

the nominal real power compensation value ΔP_0. The SACSs also share an equal frequency in a steady state leading to an identical compensation value ΔP_0 for both DGs. Consequently, the proposed SACS-SFC restores frequency accurately to the rated value while realizing equal real power sharing. Notably, the secondary control parameters shown in Table I are intended to make the PI control loop faster than the SACS control loop, hence why the frequency restoration in Fig. 18 is faster than the power sharing.

Moreover, the extracted SACS current and generated SACS voltage waveforms for both DGs are shown in Fig. 19. Based on the SACS current, shown in Fig. 19(a), it can be seen that the current magnitude of DG$_1$ decreases and DG$_2$ increases, which accords with the SACS real power waveform in Fig. 18. The effectiveness of the signal extraction can be verified, according to Fig. 19(b), in which the zoomed-in SACS current waveforms are almost pure sinusoidal without harmonics. Furthermore, the

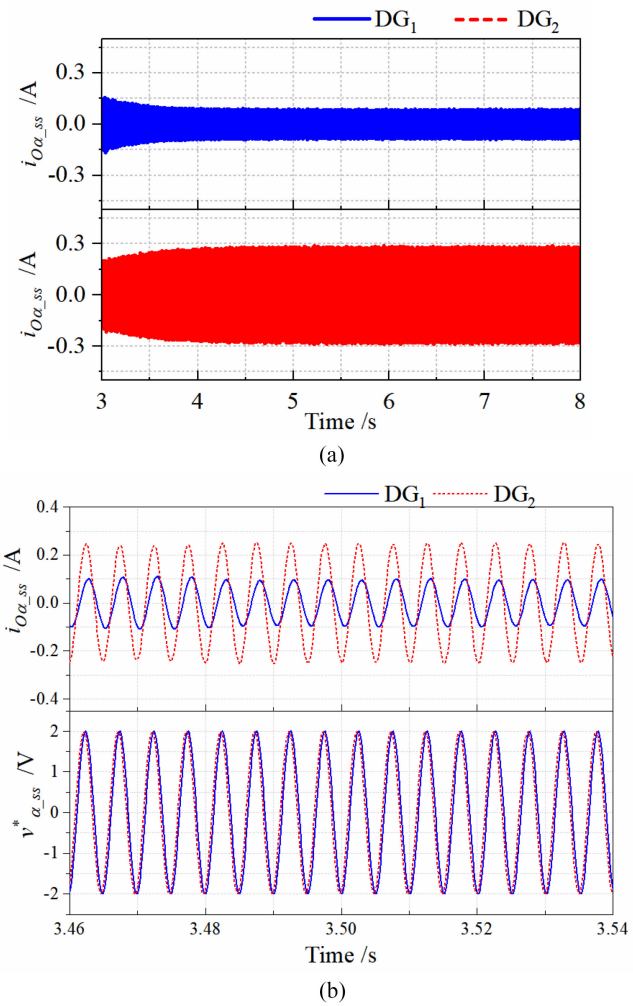

Fig. 19. Simulation waveforms of extracted SACS current and generated SACS voltage in both DGs: (a) extracted SACS current; and (b) zoomed-in waveform of SACS current and voltage.

voltage of DG_2 is leading to DG_1 as shown in the bottom of Fig. 19(b), resulting in real power flow from DG_2 to DG_1.

B. Verification of Amplification Gain Design

According to the steady-state analysis in Section IV-B, the amplification gain G_p is related to the SACS real power P_{ss}, as shown in (24). To verify this conclusion, G_p is designed to be 5000, 4000, 3000, and 2000, respectively, and the corresponding waveforms of SACS real power are plotted in Fig. 20. Note that the SACS droop gain k_{ss} should be adjusted accordingly to ensure that the dynamic model in (32) remains unchanged under each G_p value. As G_p declines, P_{ss1} declines and P_{ss2} increases coinciding with (24). However, when G_p is too small, e.g., 2000, the power-angle stability of the SACS cannot be guaranteed; therefore, the system becomes unstable as indicated by the blue curve. The steady-state analysis and design methodology of G_p can be validated through this simulation.

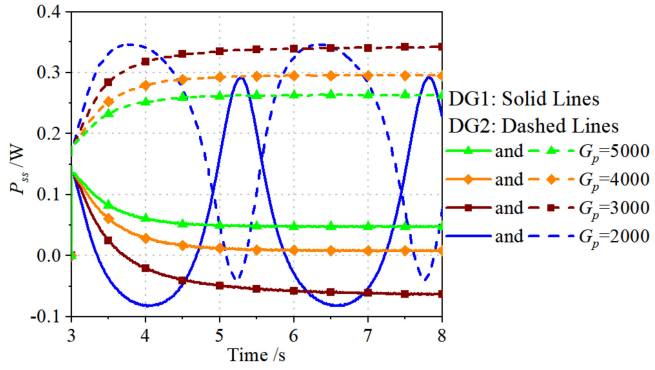

Fig. 20. Simulated waveforms of SACS real power for DG_1 and DG_2 under different amplification gains.

C. Design Verification of the SACS Droop Gain and PI Gains

As explained in Section IV-C, there are two options when designing the PI control loop and SACS control loop. The simulation results in Fig. 18 demonstrate a case, where the PI control loop is designed to be faster than the SACS control loop. The other design case (in which the SACS control loop is faster than the PI control loop) is presented in Fig. 21. The SACS droop gain k_{ss} is set to be 2.5e–3, and the integral gain $k_{i\omega}$ is set to be 1e3; other control parameters are identical to those in Table I. The system remains stable and frequency restoration and real power sharing are achieved under a steady state. Yet compared with Fig. 18, the dynamic response speed of the PI control loop and SACS control loop is exchanged. Real power sharing can be achieved quite quickly, but frequency restoration takes relatively longer. In conclusion, both design options for the PI control loop and SACS control loop are validated by the simulation results. We can choose either option to design proper SACS droop gain and PI gains according to practical requirements.

VI. Experimental Verification

Hardware experiments have been conducted to verify the effectiveness of the proposed SACS-SFC based on the microgrid prototype in Fig. 22. The system consists of four DGs and some resistive load, connected via topology similar to that in Fig. 1. Each DG is composed of a three-leg three-phase 9-kVA inverter, an *LC* filter, and feeder impedance. Detailed power-stage and control parameters are given in Table I. All control algorithms are realized through DSP TMS320F28335 from Texas Instruments. Two power analyzers (YOKOGAWA WT1804E) are used to measure the output power, frequency, and voltage and for harmonic analysis. The power analyzer outputs the measured real power and frequency through an embedded DA converter, after which a Tektronix oscilloscope (MDO3014) is used to capture the waveforms of real power and frequency.

To clearly demonstrate the effectiveness of the proposed SACS-SFC, secondary controllers based on PI-SFC and SACS-SFC are respectively implemented in the experiment. The experimental procedure is described herein. At first, all four DGs operate under conventional droop control, resulting in frequency

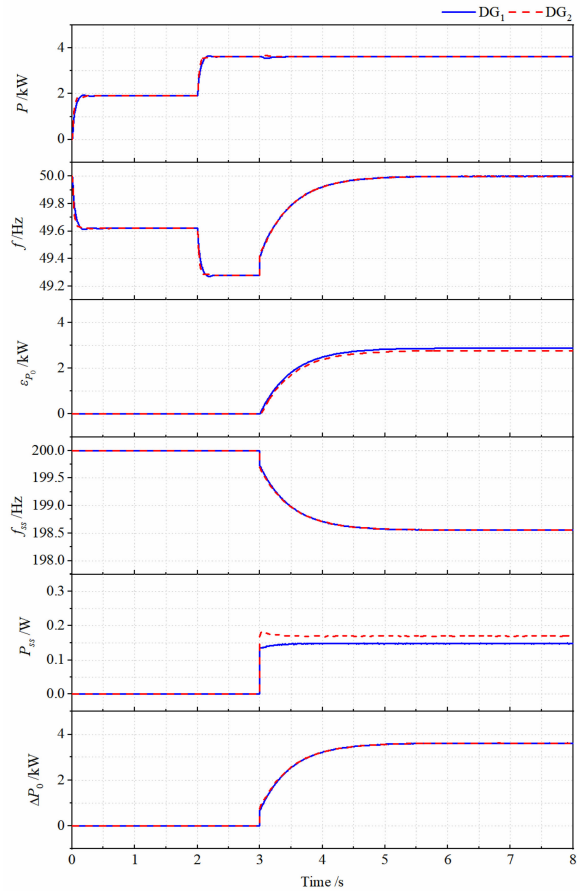

Fig. 21. Simulated waveforms of the output real power P, frequency f, output of PI regulator ε_{P_0}, SACS frequency $f_{\rm ss}$, SACS real power $P_{\rm ss}$, and compensation value of nominal real power ΔP_0 of two DGs under the proposed SACS-SFC, where the SACS control loop is designed to be faster than the PI control loop.

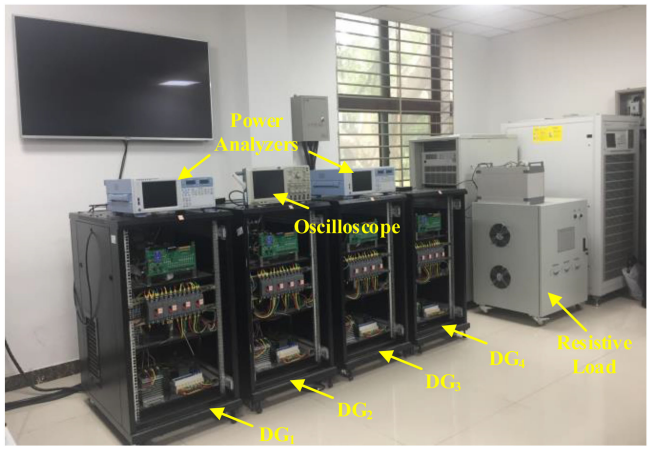

(a)

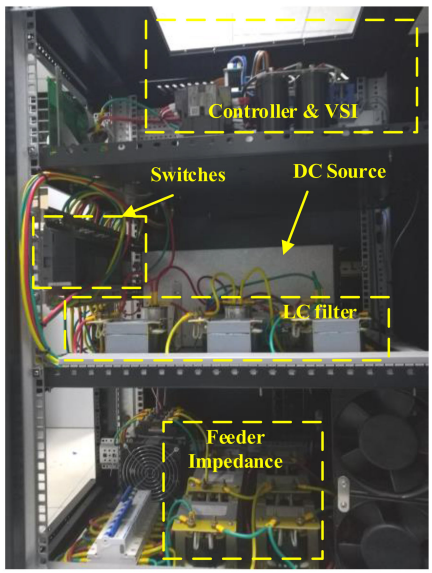

(b)

Fig. 22. Photograph of microgrid prototype: (a) system overall diagram; and (b) structure inside each DG cabinet.

deviation. Afterward, the secondary control for DG_1, DG_2, DG_3, and DG_4 is activated successively with a 60-ms time delay among each inverter to accelerate the integration error. Experimental results during this period under PI-SFC and SACS-SFC are shown in Figs. 23 and 24, respectively. Then, the scenarios of a load reduction and load increase shown in Figs. 25 and 26 are devised to further investigate the dynamic performance of the secondary controller.

The transient process from conventional droop to PI-SFC is shown in Fig. 23, and that from conventional droop to SACS-SFC appears in Fig. 24. Based on Figs. 23(a) and 24(a), the waveforms of frequency for these secondary control methods are nearly the same. Before the secondary control is activated, the frequency drops to about 49.8 Hz because only conventional droop control is implemented at this stage. Then, the secondary controller is activated. Based on Fig. 23(b), without the help of SACS, although the frequency is drawn back to the rated value of 50.00 Hz, real power is no longer evenly shared among DGs due to different activation moments of secondary control. Such a phenomenon corresponds with the analysis in Section II-B. For the results in Fig. 24, the proposed SACS-SFC is implemented and a SACS with an amplitude of 1.15 V and a nominal frequency of 200 Hz is generated by each DG. Compared with the PI-SFC, the proposed SACS-SFC can maintain equal real power sharing while restoring frequency accurately to the rated value.

To further test the performance of the secondary controller, a 5.2-kW resistive load is switched OFF and then switched ON 20 s later. Corresponding waveforms of the frequency and real power under PI-SFC and SACS-SFC are shown in Figs. 25 and 26. Each secondary control method can maintain the frequency at the rated value, even though small deviations exist in the dynamic process according to Figs. 25(a) and 26(a). The power sharing performance of the PI-SFC is obviously poor and gradually becomes worse. However, the proposed SACS-SFC can realize frequency restoration and accurate real power sharing simultaneously.

To confirm that the injected SACS does not affect voltage quality excessively, PCC voltage waveforms and the corresponding THD analysis result for PI-SFC and the proposed

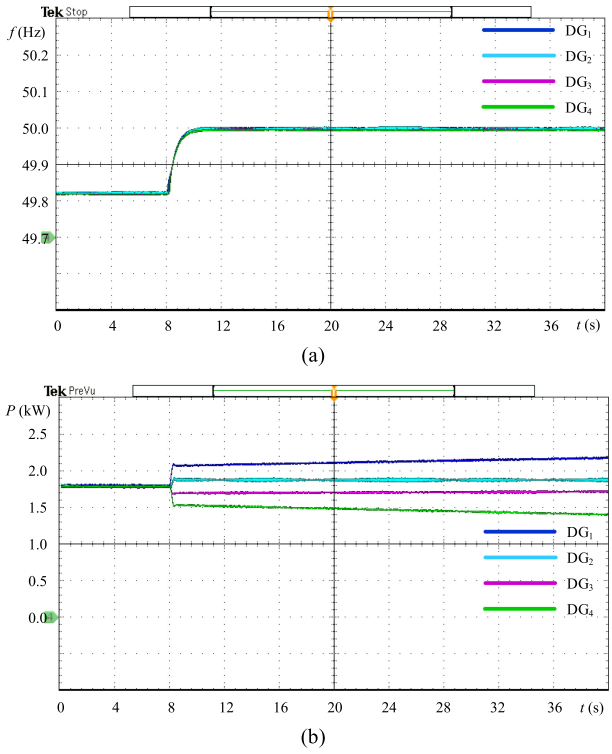

Fig. 23. Experimental waveforms of (a) frequency f and (b) output real power P of four DGs under PI-SFC.

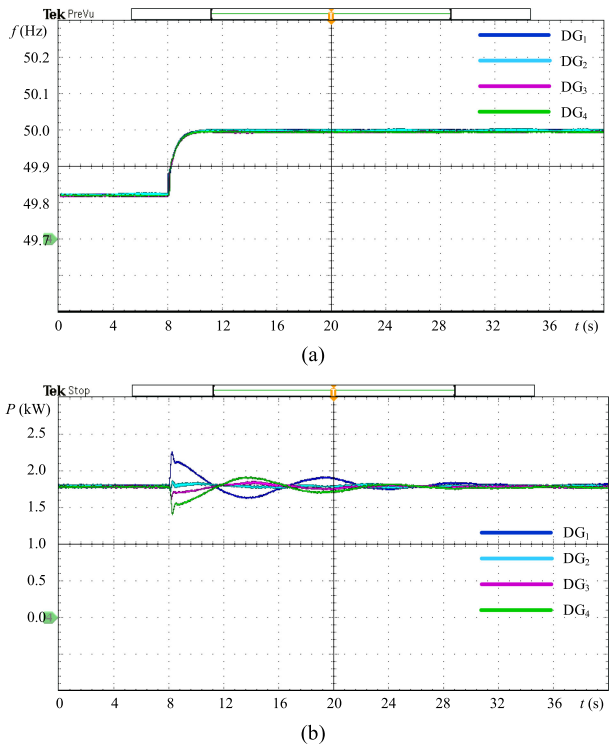

Fig. 24. Experimental waveforms of (a) frequency f and (b) output real power P of four DGs under the proposed SACS-SFC.

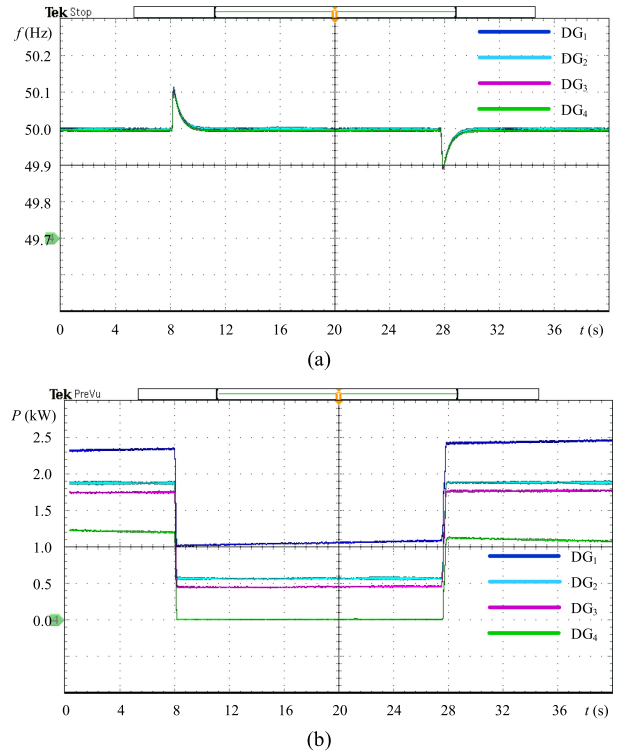

Fig. 25. Experimental waveforms of (a) frequency f and (b) output real power P of four DGs under PI-SFC during load step changes.

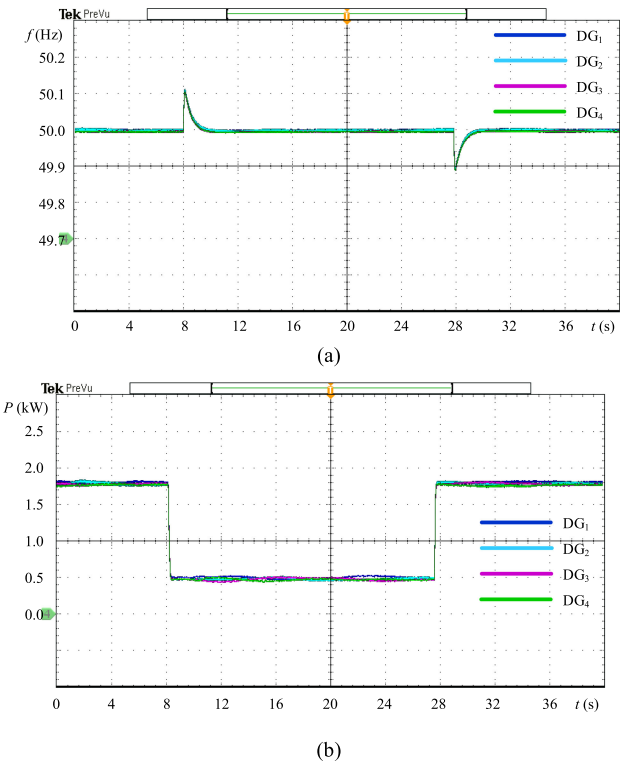

Fig. 26. Experimental waveforms of (a) frequency f and (b) output real power P of four DGs under the proposed SACS-SFC during load step changes.

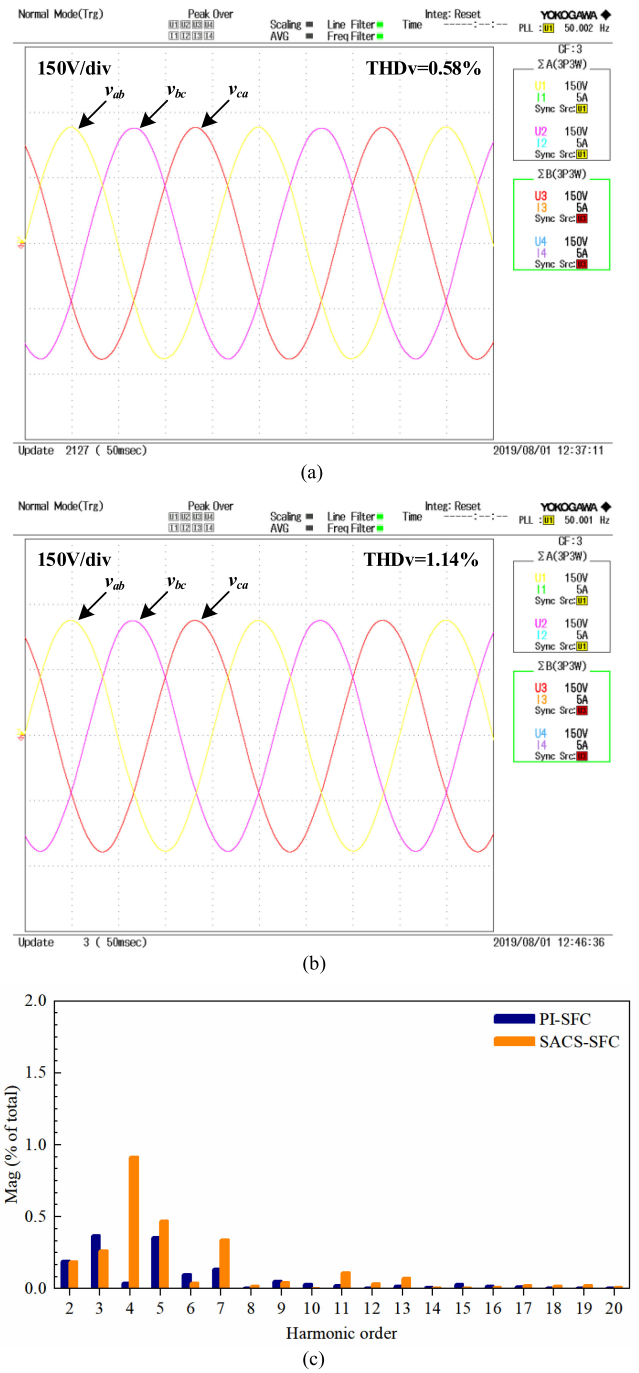

Fig. 27. PCC voltage waveforms under (a) PI-SFC, (b) SACS-SFC, and (c) THD analysis result.

SACS-SFC are displayed in Fig. 27. The THD of the proposed method is slightly higher than that of the PI-SFC, and the component of fourth harmonic voltage is clear in Fig. 27(c) for SACS-SFC due to SACS injection; however, no obvious differences appear in their time-domain waveforms. Also, the fourth-order distortion and THD of SACS-SFC are each limited within a reasonable range, which will not exceed the standard in [39].

VII. Conclusion

This article proposes a decentralized SFC method for a droop-controlled islanded microgrid based on injection of an additional SACS. In the proposed secondary control, the frequency is restored to the rated value by a PI regulator as in the existing PI-SFC. Moreover, unequal real power sharing in PI-SFC is avoided by the proposed droop relation between the frequency of the injected SACS and the compensation value of nominal real power. Therefore, the proposed SACS-SFC method restores the frequency accurately while maintains equal real power sharing among parallel DGs without the help of any communication links. Furthermore, this article provides a comprehensive design procedure for essential control parameters concerning secondary control based on steady state and dynamic model of the proposed control structure. Finally, simulation and experimental results verify the proposed control method.

References

[1] P. Piagi and R. H. Lasseter, "Autonomous control of microgrids," in *Proc. IEEE Power Eng. Soc. Gen. Meeting*, Montreal, QC, Canada, 2006, pp. 1–8.

[2] J. M. Guerrero, M. Chandorkar, T. Lee, and P. C. Loh, "Advanced control architectures for intelligent microgrids—Part I: Decentralized and hierarchical control," *IEEE Trans. Ind. Electron.*, vol. 60, no. 4, pp. 1254–1262, Apr. 2013.

[3] J. Rocabert, A. Luna, F. Blaabjerg, and P. Rodríguez, "Control of power converters in AC microgrids," *IEEE Trans. Power Electron.*, vol. 27, no. 11, pp. 4734–4749, Nov. 2012.

[4] B. Kroposki, C. Pink, R. DeBlasio, H. Thomas, M. Simões, and P. K. Sen, "Benefits of power electronic interfaces for distributed energy systems," *IEEE Trans. Energy Convers.*, vol. 25, no. 3, pp. 901–908, Sep. 2010.

[5] A. Khalil, K. A. Alfaitori, and A. Elbarsha, "Stability analysis of parallel-inverters in microgrid," in *Proc. 20th Int. Conf. Autom. Comput.*, Cranfield, U.K., 2014, pp. 110–115.

[6] J. M. Guerrero, J. C. Vasquez, J. Matas, L. G. Vicuna, and M. Castilla, "Hierarchical control of droop-controlled AC and DC microgrids—A general approach toward standardization," *IEEE Trans. Ind. Electron.*, vol. 58, no. 1, pp. 158–172, Jan. 2011.

[7] A. Bidram and A. Davoudi, "Hierarchical structure of microgrids control system," *IEEE Trans. Smart Grid*, vol. 3, no. 4, pp. 1963–1976, Dec. 2012.

[8] J. M. Guerrero, L. Hang, and J. Uceda, "Control of distributed uninterruptible power supply systems," *IEEE Trans. Ind. Electron.*, vol. 55, no. 8, pp. 2845–2859, Aug. 2008.

[9] J. M. Guerrero, J. C. Vasquez, J. Matas, M. Castilla, and L. G. de Vicuna, "Control strategy for flexible microgrid based on parallel line-interactive UPS systems," *IEEE Trans. Ind. Electron.*, vol. 56, no. 3, pp. 726–736, Mar. 2009.

[10] Y. Khayat *et al.*, "On the secondary control architectures of AC microgrids: An overview," *IEEE Trans. Power Electron.*, vol. 35, no. 6, pp. 6482–6500, Jun. 2020.

[11] X. Yang, Y. Du, J. Su, L. Chang, Y. Shi, and J. Lai, "An optimal secondary voltage control strategy for an islanded multibus microgrid," *IEEE J. Emerg. Sel. Topics Power Electron.*, vol. 4, no. 4, pp. 1236–1246, Dec. 2016.

[12] Q. Shafiee, J. M. Guerrero, and J. C. Vasquez, "Distributed secondary control for islanded microgrids—A novel approach," *IEEE Trans. Power Electron.*, vol. 29, no. 2, pp. 1018–1031, Feb. 2014.

[13] R. Heydari, T. Dragicevic, and F. Blaabjerg, "High-bandwidth secondary voltage and frequency control of VSC-based AC microgrid," *IEEE Trans. Power Electron.*, vol. 34, no. 11, pp. 11320–11331, Nov. 2019.

[14] J. W. Simpson-Porco, Q. Shafiee, F. Dörfler, J. C. Vasquez, J. M. Guerrero, and F. Bullo, "Secondary frequency and voltage control of islanded microgrids via distributed averaging," *IEEE Trans. Ind. Electron.*, vol. 62, no. 11, pp. 7025–7038, Nov. 2015.

[15] F. Guo, C. Wen, J. Mao, and Y. Song, "Distributed secondary voltage and frequency restoration control of droop-controlled inverter-based microgrids," *IEEE Trans. Ind. Electron.*, vol. 62, no. 7, pp. 4355–4364, Jul. 2015.

[16] L.-Y. Lu and C.-C. Chu, "Consensus-based secondary frequency and voltage droop control of virtual synchronous generators for isolated AC micro-grids," *IEEE J. Emerg. Sel. Topics Circuits Syst.*, vol. 5, no. 3, pp. 443–455, Sep. 2015.
[17] A. Pilloni, A. Pisano, and E. Usai, "Robust finite-time frequency and voltage restoration of inverter-based microgrids via sliding-mode cooperative control," *IEEE Trans. Ind. Electron.*, vol. 65, no. 1, pp. 907–917, Jan. 2018.
[18] N. M. Dehkordi, H. R. Baghaee, N. Sadati, and J. M. Guerrero, "Distributed noise-resilient secondary voltage and frequency control for islanded microgrids," *IEEE Trans. Smart Grid*, vol. 10, no. 4, pp. 3780–3790, Jul. 2019.
[19] V. Nasirian, Q. Shafiee, J. M. Guerrero, F. L. Lewis, and A. Davoudi, "Droop-free distributed control for AC microgrids," *IEEE Trans. Power Electron.*, vol. 31, no. 2, pp. 1600–1617, Feb. 2016.
[20] P. Wang, X. Lu, X. Yang, W. Wang, and D. Xu, "An improved distributed secondary control method for DC microgrids with enhanced dynamic current sharing performance," *IEEE Trans. Power Electron.*, vol. 31, no. 9, pp. 6658–6673, Sep. 2016.
[21] Y. R. Rodrigues, M. Abdelaziz, and L. Wang, "D-PMU based secondary frequency control for islanded microgrids," *IEEE Trans. Smart Grid*, vol. 11, no. 1, pp. 857–872, Jan. 2020.
[22] Z. Shuai, W. Huang, X. Shen, Y. Li, X. Zhang, and Z. J. Shen, "A maximum power loading factor (MPLF) control strategy for distributed secondary frequency regulation of islanded microgrid," *IEEE Trans. Power Electron.*, vol. 34, no. 3, pp. 2275–2291, Mar. 2019.
[23] M. Hua, H. Hu, Y. Xing, and J. M. Guerrero, "Multilayer control for inverters in parallel operation without intercommunications," *IEEE Trans. Power Electron.*, vol. 27, no. 8, pp. 3651–3663, Aug. 2012.
[24] H. Xin, L. Zhang, Z. Wang, D. Gan, and K. P. Wong, "Control of island AC microgrids using a fully distributed approach," *IEEE Trans. Smart Grid*, vol. 6, no. 2, pp. 943–945, Mar. 2015.
[25] H. Shi, F. Zhuo, H. Yi, F. Wang, D. Zhang, and Z. Geng, "A novel real-time voltage and frequency compensation strategy for photovoltaic-based microgrid," *IEEE Trans. Ind. Electron.*, vol. 62, no. 6, pp. 3545–3556, Jun. 2015.
[26] M. Yazdanian and A. Mehrizi-Sani, "Washout filter-based power sharing," *IEEE Trans. Smart Grid*, vol. 7, no. 2, pp. 967–968, Mar. 2016.
[27] Y. Han, H. Li, L. Xu, X. Zhao, and J. M. Guerrero, "Analysis of washout filter-based power sharing strategy—An equivalent secondary controller for islanded microgrid without LBC lines," *IEEE Trans. Smart Grid*, vol. 9, no. 5, pp. 4061–4076, Sep. 2018.
[28] P. Li, X. Wang, W. Lee, and D. Xu, "Dynamic power conditioning method of microgrid via adaptive inverse control," *IEEE Trans. Power Del.*, vol. 30, no. 2, pp. 906–913, Apr. 2015.
[29] J. M. Rey, P. Martí, M. Velasco, J. Miret, and M. Castilla, "Secondary switched control with no communications for islanded microgrids," *IEEE Trans. Ind. Electron.*, vol. 64, no. 11, pp. 8534–8545, Nov. 2017.
[30] A. Tuladhar, J. Hua, T. Unger, and K. Mauch, "Control of parallel inverters in distributed AC power systems with consideration of line impedance effect," *IEEE Trans. Ind. Appl.*, vol. 36, no. 1, pp. 131–138, Jan. 2000.
[31] B. Liu, Z. Liu, J. Liu, R. An, H. Zheng, and Y. Shi, "An adaptive virtual impedance control scheme based on small-AC-signal injection for unbalanced and harmonic power sharing in islanded microgrids," *IEEE Trans. Power Electron.*, vol. 34, no. 12, pp. 12333–12355, Dec. 2019.
[32] S. Peyghami, H. Mokhtari, P. C. Loh, P. Davari, and F. Blaabjerg, "Distributed primary and secondary power sharing in a droop-controlled LVDC microgrid with merged AC and DC characteristics," *IEEE Trans. Smart Grid*, vol. 9, no. 3, pp. 2284–2294, May 2018.
[33] T. Wu, Z. Liu, J. Liu, B. Liu, and S. Wang, "Small AC signal droop based secondary control for microgrids," in *Proc. IEEE Appl. Power Electron. Conf. Expo.*, 2016, pp. 3370–3375.
[34] M. Castilla, A. Camacho, P. Martí, M. Velasco, and M. M. Ghahderijani, "Impact of clock drifts on communication-free secondary control schemes for inverter-based islanded microgrids," *IEEE Trans. Ind. Electron.*, vol. 65, no. 6, pp. 4739–4749, Jun. 2018.
[35] E. A. A. Coelho, P. C. Cortizo, and P. F. D. Garcia, "Small-signal stability for parallel-connected inverters in stand-alone AC supply systems," *IEEE Trans. Ind. Appl.*, vol. 38, no. 2, pp. 533–542, Mar. 2002.
[36] N. Pogaku, M. Prodanovic, and T. C. Green, "Modeling, analysis and testing of autonomous operation of an inverter-based microgrid," *IEEE Trans. Power Electron.*, vol. 22, no. 2, pp. 613–625, Mar. 2007.
[37] J. He, Y. W. Li, and F. Blaabjerg, "An enhanced islanding microgrid reactive power, imbalance power, and harmonic power sharing scheme," *IEEE Trans. Power Electron.*, vol. 30, no. 6, pp. 3389–3401, Jun. 2015.
[38] P. D. Evans and P. R. Close, "Harmonic distortion in PWM inverter output waveforms," *IEE Proc. B—Elect. Power Appl.*, vol. 134, no. 4, pp. 224–232, 1987.
[39] IEEE Recommended Practice and Requirements for Harmonic Control in Electric Power Systems, IEEE Standard 519-2014 (Revision of IEEE Std 519-1992), 2014.
[40] T. Morstyn, B. Hredzak, and V. G. Agelidis, "Control strategies for microgrids with distributed energy storage systems: An overview," *IEEE Trans. Smart Grid*, vol. 9, no. 4, pp. 3652–3666, Jul. 2018.
[41] P. Rodriguez, A. Luna, I. Candela, R. Mujal, R. Teodorescu, and F. Blaabjerg, "Multiresonant frequency-locked loop for grid synchronization of power converters under distorted grid conditions," *IEEE Trans. Ind. Electron.*, vol. 58, no. 1, pp. 127–138, Jan. 2011.
[42] P. Kundur, *Power System Stability and Control*. New York, NY, USA: McGraw-Hill, 1994.
[43] Guide on Security and Stability for Power Systems, Chin. Electric Power Industry Standard DL 755-2001, 2001.
[44] J. C. Vasquez, J. M. Guerrero, M. Savaghebi, J. Eloy-Garcia, and R. Teodorescu, "Modeling, analysis, and design of stationary-reference-frame droop-controlled parallel three-phase voltage source inverters," *IEEE Trans. Ind. Electron.*, vol. 60, no. 4, pp. 1271–1280, Apr. 2013.
[45] *IEEE Standard for Interconnecting Distributed Resources With Electric Power Systems*, IEEE Standard 1547-2003, pp. 1–28, 2003.

Baojin Liu (Member, IEEE) received the B.S. degree in electrical engineering and automation from Dalian Maritime University, Dalian, China, in 2014. He is currently working toward the Ph.D. degree with Xi'an Jiaotong University, Xi'an, China.

His research interests include coordinative control of parallel inverters and power quality control in ac microgrids.

Teng Wu received the B.S. and Ph.D. degrees in electrical engineering from Xi'an Jiaotong University, Xi'an, China, in 2012 and 2017, respectively.

He is currently with Envision Energy Co., Ltd. His research mainly focused on the coordinative control of droop-based paralleled converters in ac microgrids.

Zeng Liu (Member, IEEE) received the B.S. degree from Hunan University, Changsha, China, and the M.S. and Ph.D. degrees from Xi'an Jiaotong University, Xi'an, China, in 2006, 2009, and 2013 respectively, all in electrical engineering.

He then joined XJTU as a Faculty Member in electrical engineering, where he is currently an Associate Professor. From 2015 to 2017, he was with the Center for Power Electronics Systems, Virginia Polytechnic Institute and State University, Blacksburg, VA, USA, as a Visiting Scholar. His research interests include control of power systems with multiple converters renewable energy and energy storage applications, and small-signal stability of power electronics systems.

Dr. Liu received an IEEE TRANSACTIONS ON POWER ELECTRONICS Prize Paper Award in 2016, and served as Secretary-General for *2019 IEEE 10th International Symposium on Power Electronics for Distributed Generation Systems.*

Jinjun Liu (Fellow, IEEE) received the B.S. and Ph.D. degrees in electrical engineering from Xi'an Jiaotong University (XJTU), Xi'an, China, in 1992 and 1997, respectively.

He joined the XJTU Electrical Engineering School as a faculty. From late 1999 to early 2002, he was with the Center for Power Electronics Systems, Virginia Polytechnic Institute and State University, Blacksburg, VA, USA, as a Visiting Scholar. In late 2002, he became a Full Professor and then the Head of the Power Electronics and Renewable Energy Center at XJTU, which now comprises 21 faculty members and more than 150 graduate students, and carries one of the leading power electronics programs in China. From 2005 to early 2010, he was an Associate Dean of Electrical Engineering School, XJTU, and from 2009 to early 2015, the Dean for Undergraduate Education of XJTU. He is currently a XJTU Distinguished Professor of Power Electronics. He has coauthored three books (including one textbook), published more than 400 technical papers in peer-reviewed journals and conference proceedings, holds more than 50 invention patents (China/US), and delivered for many times plenary keynote speeches and tutorials at IEEE conferences or China national conferences in power electronics area. His research interests include modeling, control, and design methods for power converters and electronified power systems, power quality control, and utility applications of power electronics, and microgrids for sustainable energy and distributed generation.

Dr. Liu received eight times governmental awards at national level or provincial/ministerial level for scientific research/teaching achievements. He also received the 2006 Delta Scholar Award, the 2014 Chang Jiang Scholar Award, the 2014 Outstanding Sci-Tech Worker of the Nation Award, and the IEEE TRANSACTIONS ON POWER ELECTRONICS 2016 Prize Paper Award. He was the IEEE Power Electronics Society Region 10 Liaison, and then, China Liaison for 10 years, an Associate Editor for the IEEE TRANSACTIONS ON POWER ELECTRONICS for 13 years, 2015–2019 Executive Vice President, and 2020–2021 Vice President for membership of IEEE PELS. He is on the Board of China Electrotechnical Society, and was elected the Vice President in 2013 and the Secretary General in 2018 of the CES Power Electronics Society. Since 2013, he has been the Vice President for International Affairs, China Power Supply Society (CPSS) and since 2016, the inaugural Editor-in-Chief of CPSS Transactions on Power Electronics and Applications. Since 2013, he has been the Vice Chair of the Chinese National Steering Committee for College Electric Power Engineering Programs.